Inorganic Chemistry
Article
Cite This: Inorg. Chem. 2018, 57, 5870−5878
pubs.acs.org/IC

Probing Fe−V Bonding in a C_3-Symmetric Heterobimetallic Complex

Samuel M. Greer,[†,‡] Johannes McKay,[†] Kathryn M. Gramigna,[§] Christine M. Thomas,[*,§,⊥] Sebastian A. Stoian,[*,†,∥] and Stephen Hill[*,†,#]

[†]National High Magnetic Field Laboratory, Florida State University, Tallahassee, Florida 32310, United States
[‡]Department of Chemistry and Biochemistry, Florida State University, Tallahassee, Florida 32306, United States
[§]Department of Chemistry, Brandeis University, Waltham, Massachusetts 02453, United States
[∥]Department of Chemistry, University of Idaho, Moscow, Idaho 83844, United States
[⊥]Department of Chemistry and Biochemistry, The Ohio State University, Columbus, Ohio 43210, United States
[#]Department of Physics, Florida State University, Tallahassee, Florida 32306, United States

Supporting Information

ABSTRACT: Direct metal−metal bonding of two distinct first-row transition metals remains relatively unexplored compared to their second- and third-row heterobimetallic counterparts. Herein, a recently reported Fe−V triply bonded species, $[V(^{i}PrNPPh_2)_3FeI]$ (**1**; Kuppuswamy, S.; Powers, T. M.; Krogman, J. P.; Bezpalko, M. W.; Foxman, B. M.; Thomas, C. M. Vanadium−iron complexes featuring metal−metal multiple bonds. *Chem. Sci.* **2013**, *4*, 3557−3565), is investigated using high-frequency electron paramagnetic resonance, field- and temperature-dependent ^{57}Fe nuclear gamma resonance (Mössbauer) spectroscopy, and high-field electron-electron double resonance detected nuclear magnetic resonance. From the use of this suite of physical methods, we have assessed the electronic structure of **1**. These studies allow us to establish the effective $\tilde{g}$ tensors as well as the Fe/V electro-nuclear hyperfine interaction tensors of the spin $S = {}^{1}/_{2}$ ground state. We have rationalized these tensors in the context of ligand field theory supported by quantum chemical calculations. This theoretical analysis suggests that the $S = {}^{1}/_{2}$ ground state originates from a single unpaired electron predominately localized on the Fe site.

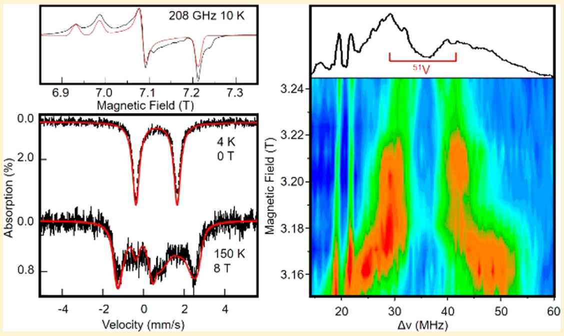

INTRODUCTION

Starting in the 1960s with the first definitive observation of chemical bonding between two transition metal ions, numerous studies have probed the reactivity and electronic structure of these compounds.[1−3] The interest in metal-metal bonding stems from both fundamental and practical perspectives. On the fundamental side, the interactions between metal centers offers a challenging environment to test electronic structure models and explore the complex relationship between structure and function.[4] From a practical perspective, metal-metal bonded systems offer a rich source of electrons for multi-electron redox reactions and, more recently, have been proposed as building blocks for molecular magnets.[5,6] Despite the prevalence of literature reporting bonding between metals, there exist relatively few examples of heterobimetallic moieties with multiple bonds. Several examples of such systems have recently been reported by our group as well as by Lu and co-workers including Ti/Co, Fe/Cr, and Ni/V species.[7−11] In these articles, vastly different ligand fields were employed for the two metal sites, resulting in molecular orbitals (MOs) that deviate from the standard σ/π/δ symmetry and instead form σ/π and nonbonding orbitals. In this manuscript, we report a detailed spectroscopic study of a triply bonded Fe−V species, $[V(^{i}PrNPPh_2)_3FeI]$ (**1**; Figure 1), where we combine ^{57}Fe nuclear gamma resonance (Mössbauer), high-frequency electron paramagnetic resonance (HFEPR), and electron-electron double resonance detected nuclear magnetic resonance (ELDOR-NMR) spectroscopy to probe the underlying electronic structure of this complex. We rationalize all of the experimental observations in terms of quantum chemical-guided ligand field theory.

MATERIALS AND METHODS

Synthesis. The compound investigated in this report is both air- and moisture-sensitive. All manipulations were performed either in an inert atmosphere glovebox or at 77 K with the sample submerged in liquid nitrogen. Compound **1** was synthesized as previously reported.[7]

^{57}Fe Nuclear Gamma Resonance (Mössbauer) Spectroscopy. The sample investigated here consisted of ∼50 mg neat polycrystalline material constrained with mineral oil in a polyethylene cup. Mössbauer spectra were collected using a Janis cryostat equipped with a built-in superconducting magnet capable of producing a maximum field of 8 T. The magnetic field was applied parallel to the propagation direction of the 14.4 keV γ-rays used to detect the Mössbauer effect. This

Received: January 31, 2018
Published: April 30, 2018

ACS Publications

DOI: 10.1021/acs.inorgchem.8b00280
Inorg. Chem. 2018, 57, 5870−5878

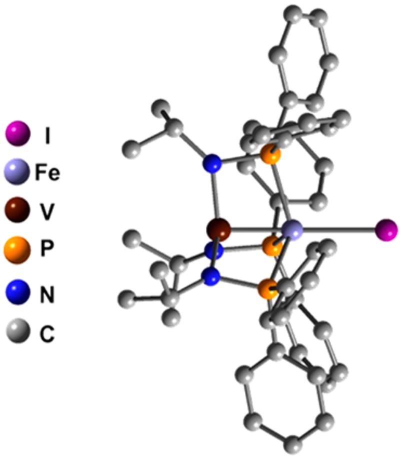

Figure 1. Molecular structure of **1**. H atoms have been omitted for clarity.

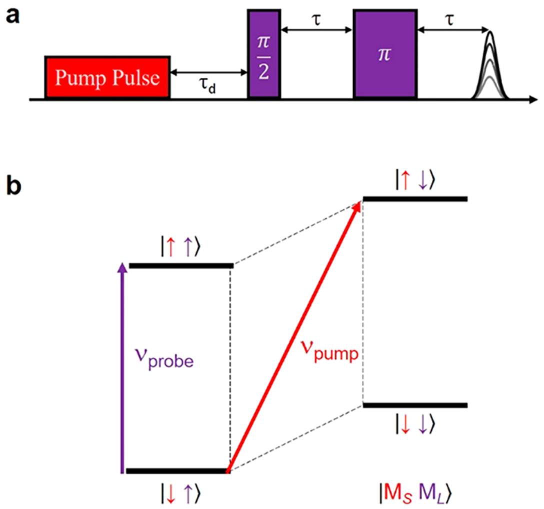

Figure 2. (a) Pulse sequence employed in the ELDOR-NMR experiment. (b) Schematic representation of the energy levels and transitions involved in the experiment: the transition shown in red corresponds to the pump pulse that drives the weakly allowed electro-nuclear zero-quantum transition (down/up to up/down); the transition highlighted in purple is monitored via the probe sequence, which measures the intensity of the allowed EPR transition ($\Delta M_S = \pm1$ and $\Delta M_I = 0$), and may be modulated via a bleaching of the ground-state population by the pump pulse. The diagram assumes $S = {}^1/_2$ and $I = {}^1/_2$; the $I > {}^1/_2$ case is discussed later.

spectrometer allowed for the recording of spectra over a temperature range of 4.2−250 K. The isomer shift is reported relative to that of α-Fe at room temperature. All spectral simulations were performed using the WMOSS software.[12]

HFEPR. Spectra were collected on microcrystalline powder samples, which were immobilized in a polyethylene cup with a Teflon stopper. The transmission-type spectrometer used in this study employed a 17 T superconducting magnet.[13] Microwave frequencies were generated in the 52−314 GHz range using a phase-locked Virginia Diodes. Inc. (Charlottesville, VA), source combined with a series of frequency multipliers. The field-modulated signal was detected by an InSb hot-electron bolometer (QMC Ltd., Cardiff, U.K.). Temperature control was realized using an Oxford Instruments (Oxford, U.K.) continuous-flow cryostat. Spectral simulations were generated using *EasySpin*.[14,15]

ELDOR-NMR. Because of the intrinsically short relaxation times of transition metal-containing compounds, pulsed electron paramagnetic resonance (EPR) experiments were carried out on a magnetically dilute sample consisting of a 5 mM solution of **1** dissolved in deuterated toluene. Measurements were performed at 8 K using a high-power, quasioptical, pulsed W-band (94 GHz) spectrometer.[16] The field-swept electron spin echo-detected EPR spectrum was recorded using the standard Hahn echo pulse sequence $(\pi/2)-\tau-(\pi)-\tau-[\text{echo}]$.[17] ELDOR-NMR measurements were performed at approximately equally spaced positions across the EPR absorption profile using the following pulse sequence: $(\text{sat})_{\text{pump}}-\tau_d-(\pi/2)_{\text{probe}}-\tau-(\pi)_{\text{probe}}-\tau-[\text{echo}]$. The first pump pulse drives a spin transition, ideally to saturation, thereby burning a hole in the inhomogeneous spin polarization profile and, hence, a hole in the EPR spectrum at the variable pump frequency, ν_{pump}. After a delay time, τ_d, the pump pulse is followed by a fixed-frequency (ν_{probe} = 94 GHz) Hahn echo detection sequence that probes any modulation of the echo intensity as ν_{pump} sweeps across the resonance;[18,19] a schematic of this experiment is shown in Figure 2. In essence, the probe pulse sequence monitors any change in the electron spin polarization caused by the saturating pump pulse. Under normal EPR conditions, this would occur when the pump and probe frequencies coincide, although spectral diffusion can result in the influence of the saturating pulse extending quite far from the pump frequency.[20] However, the saturating pulse may also drive nominally forbidden zero- and double-quantum hyperfine-coupled spin transitions involving simultaneous electron and nuclear spin flips (i.e., $\Delta M_S = \pm1$ and $\Delta M_I = \pm1$). Under such circumstances, the hole will be detected at an EPR frequency that is offset from the pump frequency by the NMR transition frequency, i.e., $\nu_{\text{pump}} - \nu_{\text{probe}} = \pm\nu_{\text{NMR}}$ (see Figure 2), hence the name ELDOR-NMR. Importantly, because the pump and probe involve excitations of the same site, ELDOR-NMR is able to detect hyperfine peak splittings that are not resolvable from inhomogeneously broadened continuous-wave (CW) EPR spectra. Moreover, in comparison to NMR, the technique inherits the high sensitivity of EPR, while simultaneously offering wide-band coverage, especially at high microwave frequencies. It is thus ideally suited to structural studies of complex coordination compounds, where unpaired electron spin density may reside on multiple dissimilar nuclear sites.

Computational Studies. We have performed a series of density functional theory (DFT) calculations using both the Gaussian 09 and ORCA v4.0 quantum chemistry software packages.[21,22] The geometry-optimized structure of the unabridged structural model was obtained at the BP86/def2-TZVP level of theory. This calculation furnished a geometry consistent with that of the X-ray structure.[23−25] Time-dependent density functional theory (TD DFT) calculations were performed at the same level of theory using the geometry-optimized structure. Both the geometry optimizations and the TD DFT calculations were performed using Gaussian 09. The electric field gradient (EFG) tensor and isomer shift were calculated using ORCA v4.0 with the BP86 functional and the following basis set combinations: CP(PPP) basis set on Fe, def2-TZVP on N/P/I, and def2-SV(P) on C/H.[26,27] State-averaged complete active space self-consistent field (SA-CASSCF) followed by second-order N-electron valence perturbation theory (NEVPT2) calculations were performed on a truncated, optimized model of **1** using the "old-dkh-tzvp" basis set. Scalar relativistic effects were accounted for by the second-order Douglas−Kroll−Hess (DKH) procedure, and the *g* factors were calculated as implemented in the ORCA v4.0 software. The active space included 10 orbitals from which 8 were σ, π, Fe^{nb}, π*, and σ* (see the text) and the remaining 2 were Fe-based 4d orbitals.

■ RESULTS

HFEPR. Spectra were recorded for a powder sample of **1** at multiple high frequencies, as shown in Figures 3 and S3. Regardless of the microwave frequency and temperature, four intense features are observed at the same *g* values ranging from ∼2.05 to 2.15, i.e., all four resonance fields exhibit a linear dependence on the microwave frequency, ν, extrapolating to ν = 0 at zero field. In other words, no zero-field contribution to the anisotropy is detected, suggesting a spin-${}^1/_2$ Kramers doublet ground state.[28] The presence of four resonances, with

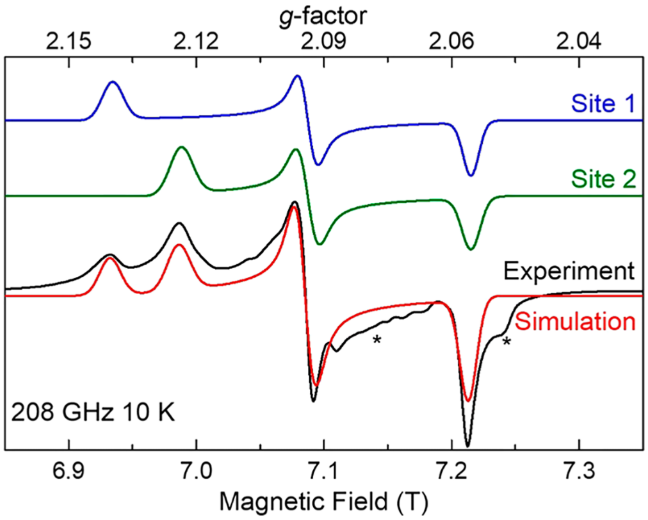

Figure 3. HFEPR spectrum of **1** recorded at 208 GHz and 10 K. The simulations shown in blue and green account for the two distinct sites in the unit cell, which are summed to arrive at the final simulation (red). Simulation parameters: $\tilde{\mathbf{g}}_1 = [2.060\ 2.098\ 2.144]$ and $\tilde{\mathbf{g}}_2 = [2.060\ 2.098\ 2.128]$ for sites 1 and 2, respectively. The features marked by * arise from a minor impurity.

an approximate 2:2:1:1 intensity ratio (from low to high g), as opposed to the maximum of three expected for a single spin-$^1/_2$ species, is accounted for by the presence of two crystallographically inequivalent sites in the unit cell: the key metric angles and bond lengths, as well as an overlay of the two geometries, are presented in Tables S1 and S2 and Figure S1. The presence of two distinct sites required us to consider two distinct sets of g values; the 2:2:1:1 intensity ratio suggests that these sites differ only in the largest (g_z) component, as seen in Figure 3.

In the absence of a metal-metal bond, the formal oxidation states of the ions are $\mathrm{V^{III}}$ and $\mathrm{Fe^{I}}$ with d^2 and d^7 electronic configurations, respectively. Together the two metal ions provide an odd number (9) of d electrons comprised by the [FeV] moiety. However, the short internuclear distance indicates a strong metal-metal bond. In turn, this interaction creates a large energy separation between the bonding and antibonding orbitals, which leads to the stabilization of an $S = {}^1/_2$, low-spin state.[29] These observations are supported by our experiments and are consistent with those previously reported, including magnetic susceptibility measurements. Thus, we analyzed the HFEPR data within the framework of the standard electronic $S = {}^1/_2$ spin Hamiltonian described by eq 1:

$$\hat{H}_{\rm elec} = \sum_k \beta_{\rm e}\vec{\mathbf{B}}\cdot\tilde{\mathbf{g}}_k\cdot\hat{\mathbf{S}}_k \tag{1}$$

where $\beta_{\rm e}$ is the electron Bohr magneton, $\vec{\mathbf{B}}$ is the magnetic field vector, $\tilde{\mathbf{g}}_k$ is the g tensor, and $\hat{\mathbf{S}}_k$ represents the total electronic spin operator. The index $k = 1, 2$ accounts for the two distinct sites in the unit cell. Our best simulation shows that the two spectral components differ only in the largest component of the individual $\tilde{\mathbf{g}}$ tensors, resulting in $g_{1z}/g_{2z} = 2.144/2.128$, $g_{1y,2y} = 2.098$, and $g_{1x,2x} = 2.060$. Figure 3 shows a representative experimental spectrum as well as the 1:1 summation of the two individual simulated sub-spectra.

^{57}Fe Nuclear Gamma Resonance (Mössbauer) Spectroscopy. Field-dependent ^{57}Fe Mössbauer spectroscopy allowed us to directly probe the electronic environment of the ^{57}Fe sites. The zero-field spectra recorded at several temperatures between 4.2 and 160 K are nearly identical and consist of a quadrupole doublet with relatively large line widths [0.45(1) mm/s; Figure S2]. The observed line width is larger than that expected for a homogeneous iron site (~0.24 mm/s), suggesting the presence of some degree of structural heterogeneity. The lack of a temperature-induced broadening demonstrates that, even at 4.2 K, the electronic spin is in a fast relaxation regime; that is, we observe a spin-flip rate higher than 10^7 Hz. The 4.2 K and 0 T spectrum is best described using an isomer shift $\delta = 0.32(1)$ mm/s and a quadrupole splitting $\Delta E_{\rm Q} = 2.14(2)$ mm/s. The quadrupole splitting is related to the principal components of the EFG tensor by

$$\Delta E_{\rm Q} = \frac{1}{2}eQV_{zz}\sqrt{1 + \frac{1}{3}\eta^2} \tag{2}$$

and

$$\eta = \frac{|V_{yy} - V_{xx}|}{V_{zz}} \tag{3}$$

where e is the elementary charge, Q is the nuclear quadrupole moment, and $V_{\mu\mu}$ ($\mu = x, y, z$) is a principal component of the EFG tensor in a coordinate system where $|V_{zz}| \geq |V_{yy}| \geq |V_{xx}|$.

The observation of a single quadrupole doublet suggests that the two distinct sites detected by HFEPR exhibit very similar zero-field parameters and cannot be differentiated by Mössbauer spectroscopy. The observation of a temperature-independent quadrupole splitting indicates that the Fe sites of **1** exhibit an isolated orbital ground state.

Figure 4 shows a series of field- and temperature-dependent spectra recorded for **1**. These spectra were analyzed using the following total spin-Hamiltonian, $\hat{H}_{\rm T,Fe}$, which was obtained by augmenting eq 1 with terms describing the hyperfine interactions of the ^{57}Fe nuclei

$$\hat{H}_{\rm T,Fe} = \hat{H}_{\rm elec} + \hat{H}_{\rm nuc,Fe} \tag{4}$$

$$\hat{H}_{\rm nuc,Fe} = \hat{\mathbf{S}}\cdot{}^{\rm Fe}\tilde{\mathbf{A}}\cdot\hat{\mathbf{I}} + \delta - \gamma_{\rm Fe}\beta_{\rm n}\vec{\mathbf{B}}\cdot\hat{\mathbf{I}} + \frac{eQV_{zz}}{4I(2I-1)}\left[3\hat{I}_z^2 - \frac{15}{4} + \eta(\hat{I}_x^2 - \hat{I}_z^2)\right] \tag{5}$$

where ${}^{\rm Fe}\tilde{\mathbf{A}}$ is the electro-nuclear hyperfine tensor, $\gamma_{\rm Fe}$ is the gyromagnetic ratio, $\beta_{\rm n}$ is the nuclear magneton, $\hat{\mathbf{I}}$ is the total nuclear spin operator, and $\hat{I}_\mu$ ($\mu = x, y, z$) are its components. Because the zero-field spectra cannot distinguish between the two molecules of the unit cell, the first term of eq 4 considers only a single site with g values that are an average of those determined from HFEPR. The observed magnetic hyperfine splitting is determined by an effective field acting on the ^{57}Fe nuclei, $\vec{\mathbf{B}}_{\rm effective} = \vec{\mathbf{B}}_{\rm internal} + \vec{\mathbf{B}}_{\rm applied}$, where the internal field generated by the unpaired electrons is given by $\vec{\mathbf{B}}_{\rm internal} = -{}^{\rm Fe}\tilde{\mathbf{A}}\cdot\langle\hat{\mathbf{S}}\rangle/\gamma_{\rm Fe}\beta_{\rm n}$. The low spin expectation values, $|\langle\hat{\mathbf{S}}\rangle| \leq 0.5$, lead to a relatively small internal field (Figure S4). Because of this behavior, some of the spectral features can only be resolved by applying a large magnetic field. At high temperature ($T > 100$ K), the Curie behavior of **1**, $\langle\hat{\mathbf{S}}\rangle \sim \frac{1}{T}$, leads to a regime where the field-dependent spectra are in effect determined by the nuclear Zeeman and quadrupolar interactions (last two terms of eq 5). Therefore, analysis of the 150 K and 8 T spectrum permits us to establish that $\Delta E_{\rm Q}$ is positive and the asymmetry parameter of the EFG tensor $\eta =$

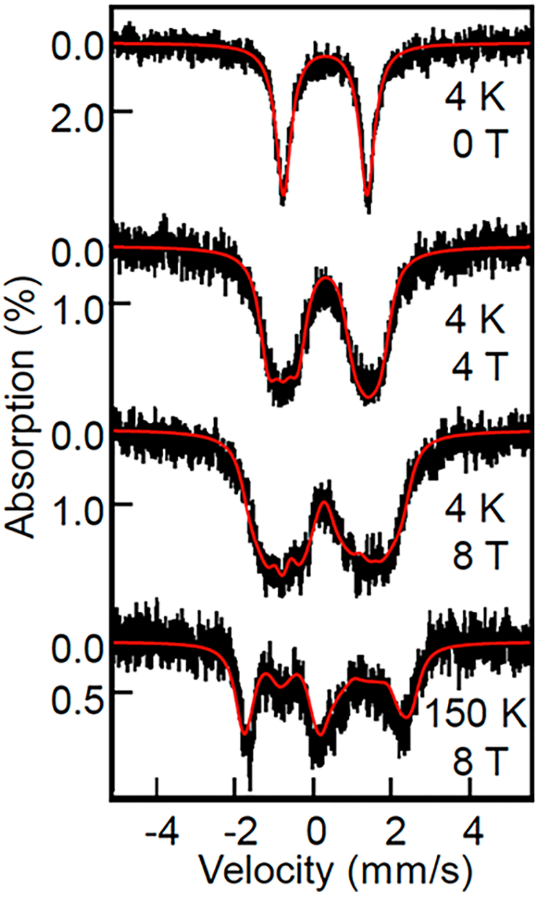

Figure 4. Experimental (black) and simulated (red) Mössbauer spectra of **1**. The spectral simulations shown here were obtained using the parameters reported in Table 1.

Table 1. Spin Hamiltonian Parameters[a] for 1

parameter	value
g_x	2.0975(5)
g_y	2.0599(5)
g_z	2.1355(5)[b]
δ (mm/s)	0.32(1)
ΔE_Q (mm/s)	2.13(1)
η	0.51(1)
α_{EFG} (deg)	35(5)
β_{EFG} (deg)	45(5)
${}^{Fe}A_x$ (MHz)	0(1)
${}^{Fe}A_y$ (MHz)	−16.6(1)
${}^{Fe}A_z$ (MHz)	−34.5(1)
$\lvert {}^{V}A_x \rvert$ (MHz)	10(3)
$\lvert {}^{V}A_y \rvert$ (MHz)	12(3)
$\lvert {}^{V}A_z \rvert$ (MHz)	28(5)

[a] Numbers in parentheses are the estimated uncertainties in the last digit. [b] The g_z value of **1** was taken as the average of the two unique sites shown in Figure 3.

0.5. When looking at the field-dependent, low-temperature spectra, knowledge of the EFG parameters allowed us to focus on assessing the magnitude of the hyperfine coupling (${}^{Fe}\tilde{\mathbf{A}}$) tensor components. Surprisingly, we found that the experimental spectra can be reproduced only by considering a highly anisotropic ${}^{Fe}\tilde{\mathbf{A}}$ tensor, for which one of the principal components is essentially zero (Table 1). Moreover, our extensive fits of the entire set of spectra suggest that the EFG and ${}^{Fe}\tilde{\mathbf{A}}$ tensors are not collinear. Figure 4 shows a series of simulations obtained using our best set of parameters listed in Table 1.

^{51}V Hyperfine Coupling Probed by ELDOR-NMR. Because neither ^{57}Fe Mössbauer nor CW EPR spectroscopy was able to illuminate the hyperfine interactions involving the V site, we turned to ELDOR-NMR to gain a measure of the level of unpaired spin density on the V site. The echo-detected, field-swept spectrum recorded at 8 K showed that the frozen solution-state g values of **1** vary only slightly from those observed in the powder spectra, $g_{z,\mathrm{soln}} = 2.12$, $g_{y,\mathrm{soln}} = 2.10$, and $g_{x,\mathrm{soln}} = 2.06$.

A 2D false color plot spanning the range of the experimentally observed ^{51}V ELDOR-NMR spectrum is shown in Figure 5; an intense (red) signal indicates strong electron depolarization due to the saturation pulse, as detected by the spin−echo sequence, where $\Delta\nu$ corresponds to the difference between these frequencies, $\nu_{\mathrm{pump}} - \nu_{\mathrm{probe}}$. For cases where the hyperfine coupling is small compared to the nuclear Zeeman interaction, one expects to observe a pair of resonances for each coupled nucleus, centered at the bare nuclear Larmor frequency and split by $A_{\mu\mu}/h$. This can be seen from the total interaction Hamiltonian, $\hat{H}_{\mathrm{T,Fe-V}}$, describing the coupled electron/vanadium nuclear pair:

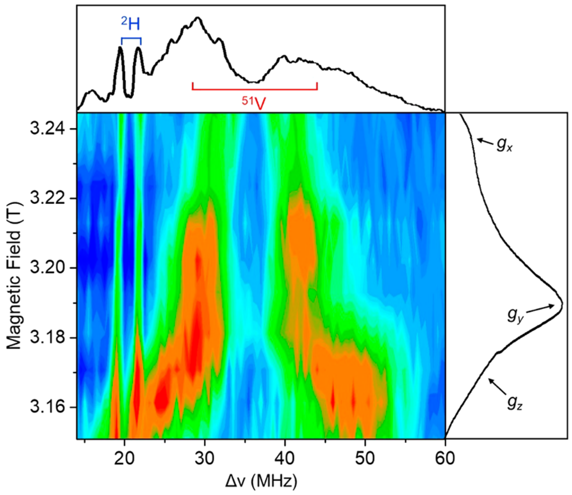

Figure 5. 2D color plot of the experimental ELDOR-NMR spectra of **1**. Red and blue correspond to high and low intensities, respectively. The right panel shows the echo-detected EPR spectrum recorded at 8 K and 94 GHz. The top panel contains a single ELDOR-NMR trace recorded at ∼3.19 T. The isotropic transition centered at $\Delta\nu \sim 20$ MHz accounts for the interaction between the unpaired electron spin density and the deuterated solvent. The axial features centered at $\Delta\nu \sim 35$ MHz arise from the V hyperfine interaction and, in the weak interaction limit, are centered at the ^{51}V nuclear Larmor frequency, and then split by the magnitude of the hyperfine coupling, which is anisotropic (different splitting for excitation at different components of the $\tilde{\mathbf{g}}$ tensor).

$$\hat{H}_{\mathrm{T,Fe-V}} = \hat{H}_{\mathrm{elec}} + \hat{H}_{\mathrm{nuc,V}} \tag{6}$$

$$\hat{H}_{\mathrm{nuc,V}} = \hat{\mathbf{S}}\cdot{}^{\mathrm{V}}\tilde{\mathbf{A}}\cdot\hat{\mathbf{I}} - \gamma_{\mathrm{V}}\beta_{\mathrm{n}}\vec{\mathbf{B}}\cdot\hat{\mathbf{I}} \tag{7}$$

where the first term in eq 6 is given by eq 1. For the simplest case with $S = I = {}^{1}/_{2}$, these expressions result in EPR transitions ($\Delta M_S = \pm 1$ and $\Delta M_I = 0$) at energies $h\nu_{\mathrm{probe}} = g\beta_e B \pm {}^{1}/_{2}A$ and weakly allowed zero- and double-quantum electro-nuclear

DOI: 10.1021/acs.inorgchem.8b00280
Inorg. Chem. 2018, 57, 5870−5878

transitions ($\Delta M_S = \pm 1$ and $\Delta M_I = \pm 1$) at $h\nu_{\mathrm{pump}} = g\beta_e B \pm \gamma\beta_n B$; hence, $h\Delta\nu = \gamma\beta_n B \pm {}^1/_2 A$.

Examination of Figure 5 reveals two strong, broad signals centered at a Larmor frequency of ~35 MHz at 3.15 T, corresponding to a gyromagnetic ratio of ~7 × 10^7 rad/s·T, as expected for the ^{51}V nucleus. The change in separation of the two ^{51}V signals as a function of the field results from an anisotropic $^{V}\tilde{\mathbf{A}}$ tensor. By driving transitions in different regions of the EPR spectrum (Figure 5, right panel), one can selectively probe the different molecular orientations and, therefore, study the hyperfine interaction as a function of the $\tilde{g}$ tensor components. Examination of Figure 5 reveals that the magnitude of the ^{51}V hyperfine coupling (the splitting between the two ^{51}V signals) decreases as the magnetic field increases, indicating that the $^{V}\tilde{\mathbf{A}}$ tensor is coaxial with the $\tilde{g}$ tensor, with the largest A and g components parallel to one another. Quantitatively, the ^{51}V ELDOR-NMR spectrum can be fit to eqs 6 and 7 (Figure S5), resulting in the principal components of the hyperfine tensor: $|^{V}A_z| = 28$, $|^{V}A_y| = 12$, $|^{V}A_x| = 10$, and $|^{V}A_{\mathrm{avg}}| = 16.7$ MHz. Meanwhile, the isotropic feature centered at ~20 MHz at 3.15 T (gyromagnetic ratio of ~4 × 10^7 rad/s·T) can be assigned to solvent deuterium interacting with the unpaired spin. Additional resonances observed in the full ELDOR-NMR spectrum (Figures S6 and S7) can be attributed to isotropic H and anisotropic N interactions. No features could definitively be assigned to hyperfine interactions involving ^{127}I ($I = {}^5/_2$, 27 MHz at 3.15 T, 100% natural abundance) or ^{31}P ($I = {}^1/_2$, 54 MHz at 3.15 T, 100% natural abundance), which could be due to the limited available bandwidth (~±200 MHz), poorly resolved/overlapping signals at low $\Delta\nu$, or electron−nuclear couplings that are too weak to efficiently facilitate the forbidden transitions. The absence of signals from Fe-based interactions is due to the low natural abundance of ^{57}Fe (~2%), which highlights the benefits of applying multiple resonance techniques to investigate this and related compounds.

The preceding analysis assumes $S = I = {}^1/_2$. However, ^{51}V has a nuclear moment of $I = {}^7/_2$ (~100% natural abundance). In a standard CW EPR spectrum, one would expect $2I + 1$ separate peaks, split by the hyperfine interaction (selection rule $\Delta M_S = \pm 1$ and $\Delta M_I = 0$), one for each of the $2I + 1$ nuclear spin projections. In contrast, the ELDOR-NMR signals arise when the pump pulse drives either a zero ($\Delta M_S = \pm 1$ and $\Delta M_I = \mp 1$) or double ($\Delta M_S = \pm 1$ and $\Delta M_I = \pm 1$) quantum transition. Consequently, to lowest order, the pump frequency is always shifted from the EPR frequency by $\Delta\nu = (\gamma\beta_n B \pm {}^1/_2 A)/h$, resulting in just two branches of overlapping signals.[18,19] With the addition of higher-order terms, e.g., nuclear quadrupole splitting, the two branches may be further split according to the nuclear spin projection M_I. Indeed, it is highly likely that such additional splitting is unresolved in Figure 5 and that, along with g strain, it plays an important role in the broad, anisotropic line width of the ^{51}V ELDOR-NMR signal. A summary of the spin-Hamiltonian parameters obtained from the HFEPR, Mössbauer, and ELDOR-NMR measurements is given in Table 1 (and Tables S3 and S6).

■ DISCUSSION

Qualitative Bonding Diagram. To aid in our interpretation, we start by constructing a qualitative MO energy level diagram (Figure 6). We begin by assuming that both the local V and Fe sites, and the overall molecule, exhibit a C_{3v} point-group symmetry and that the 3-fold rotation axis is coincident with the internuclear axis. When the metal-metal interaction is neglected, the trisamide coordination of the V$^{\mathrm{III}}$ d^2 site leads to a splitting of the five d orbitals into a singlet, a$_1$ {z^2}, and two doublets, 1e {yz, xz} and 2e {xy, $x^2 - y^2$}. In this case, we expect the a$_1$ singlet to be lowest in energy. The Fe$^{\mathrm{I}}$ d^7 site exhibits a distorted tetrahedral local geometry, for which the iodide is found along the C_3 axis. Similar to the V site, we expect the Fe 3d orbitals to be split into a singlet (a$_1$) and two doublets (1e and 2e). However, the interaction of the a$_1$ orbital with the iodide should lead to its destabilization with respect to one of the e sublevels. The magnitude of the orbital crystal field splitting will depend on both the nature and number of coordinating atoms and on the oxidation states of the central metal ions. In general, it is expected that the phosphine ligand will engender a larger splitting than the amide. However, the tetrahedral coordination geometry will have significantly less metal-ligand orbital overlap compared to that of the trigonal planar site, resulting in a weaker ligand field splitting. Additionally, it is empirically observed that the ligand field splitting increases as the oxidation state rises because it increases with the effective charge of the metal cation.[30] The lower formal charge and local coordination environment of the Fe$^{\mathrm{I}}$ site leads us to assume a substantially weaker ligand field for this site than for the V$^{\mathrm{III}}$ ion. These assumptions are validated by TD DFT calculations performed on the two mononuclear analogues of **1** (Figure S9). The difference in ligand field strength of the two ligand environments is represented qualitatively by the relative splittings on the left and right sides of the diagram in Figure 6.

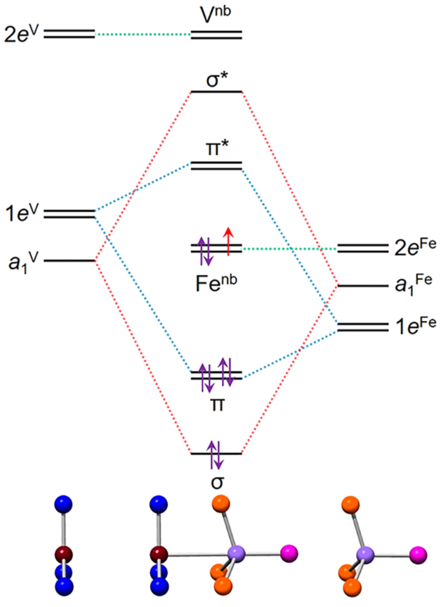

Figure 6. (Center) Qualitative MO energy level diagram of **1**. The superscript nb indicates that the orbital originates from the indicated metal and is non-bonding. (Left) Relative d-orbital splitting for a transition metal occupying a trigonal-planar coordination site. (Right) Relative d-orbital splitting for a transition metal occupying a pseudotetrahedral site. The diagram below each energy level diagram represents the corresponding metal−ligand unit, using the same color scheme as Figure 1.

Knowledge of the local d-orbital splitting allows us to consider the formation of an intermetallic bond. The stabilization of an Fe−V bond requires three conditions to be met: (i) a short internuclear distance; (ii) the presence of

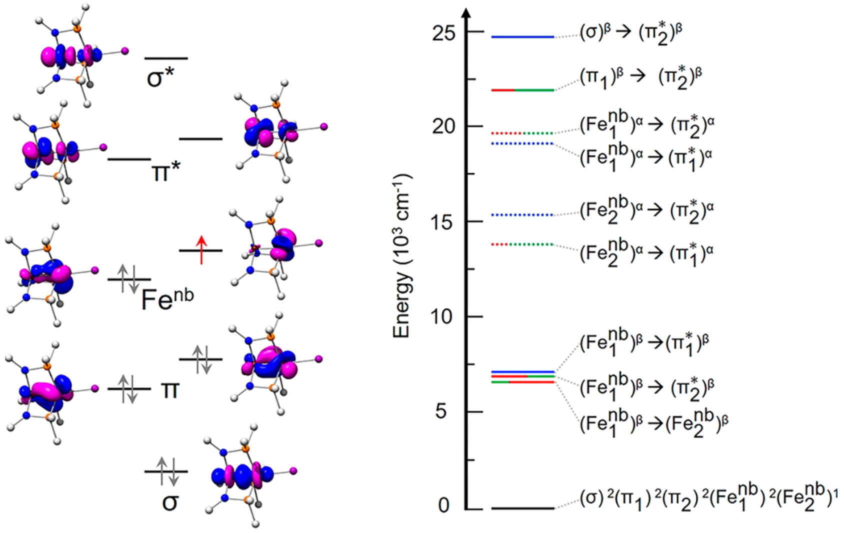

Figure 7. (Left) Qualitative MO diagram resulting from a SA-CASSCF/NEVPT2 calculation depicting the dominant configuration of the ground state. For clarity, the 4d orbitals (see Figure S12) are omitted. (Right) Energies of the first 10 states, where the labels of the excited states correspond to the single excitation that describes the main configuration of the indicated excited state. The ground state is labeled with the dominant configuration. The lines representing the energies of the states are colored according to their contribution to the $\tilde{\mathbf{g}}$ tensor: red (z), blue (y), and green (x). In the case of states that contribute to multiple components of $\tilde{\mathbf{g}}$, lines are divided into the fractions of the calculated reduced spin-orbit coupling matrix element for each Cartesian component. Solid lines denote a β-electron transition, a contribution to $\Delta g_\mu > 0$, and the dashed lines indicate an α-electron transition, a contribution to $\Delta g_\mu < 0$. The g values for this model at this level of theory are $g_x = 2.027$, $g_y = 2.085$, and $g_z = 2.200$.

orbitals with the same symmetry at both sites; (iii) comparable energies of the interacting orbitals. These criteria allow for mixing of the a_1 and 1e orbitals of the two metal sites, leading to the formation of a σ and two π bonds, respectively. Concomitantly, the large energy difference of the 2e orbital sets, combined with the long internuclear distance relative to the radial extension of the 3d orbitals between the two metal ions, impedes the formation of δ bonds. These interactions lead to the qualitative MO diagram shown in Figure 6. Subsequently, the nine available electrons fill this diagram either by following Hund's rules (to yield an $S = {}^9/_2$ ground state) or by enforcing a low-spin electronic configuration (to yield an $S = {}^1/_2$ state). The experimental data demonstrate a low-spin configuration in which the singly occupied orbital is best described as non-bonding and associated with the Fe site.

Analysis of the ^{57}Fe and ^{51}V Hyperfine Structures. Using the above model, we attempt to rationalize the observed hyperfine structure parameters vide infra. The effective $\tilde{\mathbf{A}}$ tensors can be decomposed into three contributions: the Fermi contact ($\tilde{\mathbf{A}}_{\mathrm{Fc}}$),[31] spin dipolar ($\tilde{\mathbf{A}}_{\mathrm{dip}}$), and orbital ($\tilde{\mathbf{A}}_{\mathrm{L}}$), i.e.,

$$\tilde{\mathbf{A}} = \tilde{\mathbf{A}}_{\mathrm{Fc}} + \tilde{\mathbf{A}}_{\mathrm{dip}} + \tilde{\mathbf{A}}_{\mathrm{L}} \tag{8}$$

Taking the average of the ^{51}V $\tilde{\mathbf{A}}$-tensor components removes the traceless spin-dipolar contribution and results in the pseudo-contact hyperfine coupling ($\tilde{\mathbf{A}}_{\mathrm{Fc}} + \tilde{\mathbf{A}}_{\mathrm{L}}$).[32] Given the relatively small electron density on V, we can make the simplifying assumption that $^{\mathrm{V}}\tilde{\mathbf{A}}_{\mathrm{L}}$ is negligible and that the isotropic $^{\mathrm{V}}A_{\mathrm{Fc}} \approx {}^{\mathrm{V}}A_{\mathrm{avg}} = 16.7$ MHz. To put this observation into perspective, we can compare this value with that of the mononuclear hexaquavanadium(III) compound, for which $A_{\mathrm{avg}} \sim 250$ MHz.[33] A direct comparison with this value is misleading because the present case involves a dimer of interacting spins, which means that the hexaquavanadium(III) interaction should be scaled by a projection coefficient (${}^2/_3$), resulting in $A_{\mathrm{avg}} = \sim 170$ MHz. Thus, the observed $^{\mathrm{V}}A_{\mathrm{avg}} = 16.7$ MHz demonstrates a small unpaired electron spin density on the V site, in spite of the formation of the direct Fe−V bond, i.e., the single unpaired electron is essentially localized on the Fe site. The contributions to $^{\mathrm{Fe}}\tilde{\mathbf{A}}$ may also be decomposed, as shown in eq S1 and Figure S8, revealing $^{\mathrm{Fe}}A_{\mathrm{Fc}} = -22.4$ MHz.[34] A direct comparison of the relative magnitudes of A_{Fc} for the ^{51}V and ^{57}Fe nuclei is misleading because of the large differences in the nuclear gyromagnetic ratio. However, comparing the ratios of $^{\mathrm{M}}A_{\mathrm{Fc}}/(\gamma_{\mathrm{M}}/2\pi)$ does offer a measure of the relative spin density present on each atom. The experimentally determined $|^{\mathrm{Fe}}A_{\mathrm{Fc}}/(\gamma_{\mathrm{Fe}}/2\pi)| \approx 16.0$ T and $|^{\mathrm{V}}A_{\mathrm{Fc}}/(\gamma_{\mathrm{V}}/2\pi)| \approx 1.5$ T values therefore suggest that the Fe-based unpaired spin density is one order of magnitude larger than the V one.

While the isomer shift of **1** compares well with those of analogous compounds reported by Lu and co-workers, the quadrupole splitting is significantly smaller (~2 vs ~4 mm/s). This difference can be rationalized by the difference in the ligand scaffolding used in each case. The Fe site of the analogous complex [FeVL]X,[2] where L = N[o-[NCH$_2$P(^{i}Pr)$_2$]-C$_6$H$_4$]$_3$ and X = BPh$_4$ or PF$_6$, exhibits a trigonal planar coordination environment. Planar coordination environments generate a large negative ligand contribution to the EFG along the z direction (in this case along the internuclear axis), V_{zz}. In **1**, this contribution is dramatically reduced, but not canceled, by the additional charge of the neighboring iodide, as well as the increased I−Fe−P angle (Tables S4 and S5). The diminished ligand contribution to V_{zz} results in a smaller ΔE_{Q} value for **1** compared to the related [FeVL]X compound.[2] We have further investigated the observed isomer shift and quadrupole splitting parameters using DFT: the predicted values are $\delta^{\mathrm{calc}} = 0.11$ mm/s, $\Delta E_{\mathrm{Q}}^{\mathrm{calc}} = 1.57$ mm/s, and $\eta = 0.28$. The Löwdin spin-population analysis reveals a substantial covalent reduction at each site: 1.73 α electrons for the Fe (3 expected in the free ion) and −0.85 β electrons for the V (2 in the free ion). As has been discussed by several groups, the calculated spin densities of a broken-symmetry state are unphysical.[35,36] To overcome this, we can investigate the overlap of the α and β spaces by examining the corresponding orbitals of the broken-symmetry solution, which show a nearly complete overlap of the α and β spaces (overlap = 0.85−1.00) for all orbitals with the exception of a single excess α-space orbital, identified as an $\mathrm{Fe}^{\mathrm{nb}}$ orbital, in accordance with our qualitative MO analysis (Figure S10). It has also been shown that the calculated spin densities are highly dependent on the amount of Hartree−Fock (HF) exchange in the functional.[37] We have examined this effect by performing several geometry optimizations of a truncated model compound using varying amounts of exact exchange in the functional, and we have found that a functional with 5% HF exchange produces a geometry with vanishing spin density on the V site and density approaching unity at the Fe site (Figure S11).

Electronic Origin of the $\tilde{\mathbf{g}}$ Anisotropy. The DFT-predicted g values, at the BP86/def2-TZVP level of theory from the solutions of the coupled-perturbed self-consistent field (SCF) equations, are $g_x = 2.083$, $g_y = 2.123$, and $g_z = 2.157$. While the good agreement between the DFT-predicted values and those observed experimentally is reassuring, particularly with regard to the rhombicity of the $\tilde{\mathbf{g}}$ tensor, it is instructive to develop a ligand field model to account for the observed shifts from the free electron value, $g_{\mathrm{e}} = 2.0023$. These shifts are governed by spin-orbit coupling interactions. Using the second-order perturbation formalism, the components of the $\tilde{\mathbf{g}}$ tensor may be derived through the following relationship:[38]

$$g_\mu = g_{\mathrm{e}} + \frac{1}{S}\sum_{\Theta=\mathrm{Fe,V}} \zeta_\Theta \sum_i \sum_j \Delta_{ij}^{-1}(-1)^{p_{ij}} \langle\varphi_i|{}^{\Theta}\hat{L}_\mu|\varphi_j\rangle\langle\varphi_j|{}^{\Theta}\hat{L}_\mu|\varphi_i\rangle \tag{9}$$

where g_μ is a Cartesian component of the $\tilde{\mathbf{g}}$ tensor, ζ_Θ is the one-electron spin-orbit coupling constant for Θ (=Fe or V), $p_{ij} = 0$ if the transition between states φ_i and φ_j involves a β electron and $p_{ij} = 1$ for an α electron, Δ_{ij} is the energy separation between the ith and jth states, and ${}^{\Theta}\hat{L}_\mu$ is the Cartesian component of the orbital angular momentum operator relative to nucleus Θ. An immediate implication of this equation is that the sign of Δg_μ ($g_\mu - g_{\mathrm{e}}$) is determined by the competition of the low-energy α- and β-electron transitions. If the low-lying excited states are predominately accessed via transitions involving α electrons, then $\Delta g_\mu < 0$; however, those involving low-lying β electrons will result in $\Delta g_\mu > 0$. To glean insight into the nature of the low-energy transitions that will dominate $\tilde{\mathbf{g}}$, a SA-CASSCF/NEVPT2 calculation was performed on a truncated model of **1** (Figure 7).

The significant difference between the calculated MOs in Figure 7 and the qualitative diagram in Figure 6 is the large splitting of nonbonding Fe-based orbitals ($\mathrm{Fe}^{\mathrm{nb}}$), i.e., the 2e orbital set. This splitting results from the deviation of the structure from ideal C_3 symmetry, with the largest deviation arising from the asymmetric P−Fe−P angles, which, for the two sites, are {110.5° 120.9° 108.4°} and {112.9° 117.7° 108.2°}. This can explain both the rhombic nature of the experimentally determined $\tilde{\mathbf{g}}$ tensor(s) and the differences observed for the inequivalent sites in the unit cell. Using the three lowest calculated excited states and the scheme in Figure 6 as a guide, we can write down a qualitative MO composition as follows:

$$|\mathrm{Fe}_1^{\mathrm{nb}}\rangle = \Gamma_{xy}^{\mathrm{Fe}}|\mathrm{d}_{xy}^{\mathrm{Fe}}\rangle + \Gamma_{yz}^{\mathrm{Fe}}|\mathrm{d}_{yz}^{\mathrm{Fe}}\rangle \tag{10a}$$

$$|\mathrm{Fe}_2^{\mathrm{nb}}\rangle = \Gamma_{x^2-y^2}^{\mathrm{Fe}}|\mathrm{d}_{x^2-y^2}^{\mathrm{Fe}}\rangle + \Gamma_{xz}^{\mathrm{Fe}}|\mathrm{d}_{xz}^{\mathrm{Fe}}\rangle \tag{10b}$$

$$|\pi_1{}^*\rangle = \Xi_{xy}^{\mathrm{Fe}}|\mathrm{d}_{xy}^{\mathrm{Fe}}\rangle + \Xi_{yz}^{\mathrm{Fe}}|\mathrm{d}_{yz}^{\mathrm{Fe}}\rangle + \Xi_{yz}^{\mathrm{V}}|\mathrm{d}_{yz}^{\mathrm{V}}\rangle \tag{10c}$$

$$|\pi_2{}^*\rangle = \Xi_{x^2-y^2}^{\mathrm{Fe}}|\mathrm{d}_{x^2-y^2}^{\mathrm{Fe}}\rangle + \Xi_{xz}^{\mathrm{Fe}}|\mathrm{d}_{xz}^{\mathrm{Fe}}\rangle + \Xi_{xz}^{\mathrm{V}}|\mathrm{d}_{xz}^{\mathrm{V}}\rangle \tag{10d}$$

where Ξ and Γ are fractional coefficients of the d orbitals forming the indicated MO. We note that the Fe-site contributions to these MOs are complicated by displacement of the Fe atom from the plane formed by the three P atoms. Such a geometry results in significant mixing of the d_{xy}- and d_{yz}-type orbital sets. Using the expressions in eqs 10a−10d along with eq 9, we find the following expressions for the change in $\tilde{\mathbf{g}}$ from the free electron value:

$$\Delta g_x \cong 2\zeta^{\mathrm{Fe}}\left[\frac{(\Gamma_{xy}^{\mathrm{Fe}}\Xi_{xz}^{\mathrm{Fe}} + \Gamma_{yz}^{\mathrm{Fe}}\Xi_{x^2-y^2}^{\mathrm{Fe}})^2}{\Delta_{\pi_2^*,\mathrm{Fe}_1^{\mathrm{nb}}}} + \frac{(\Gamma_{xy}^{\mathrm{Fe}}\Gamma_{xz}^{\mathrm{Fe}} + \Gamma_{x^2-y^2}^{\mathrm{Fe}}\Gamma_{yz}^{\mathrm{Fe}})^2}{\Delta_{\mathrm{Fe}_2^{\mathrm{nb}},\mathrm{Fe}_1^{\mathrm{nb}}}}\right] \tag{11a}$$

$$\Delta g_y \cong 2\zeta^{\mathrm{Fe}}\left[\frac{(\Gamma_{xy}^{\mathrm{Fe}}\Xi_{yz}^{\mathrm{Fe}} - \Gamma_{yz}^{\mathrm{Fe}}\Xi_{xy}^{\mathrm{Fe}})^2}{\Delta_{\pi_1^*,\mathrm{Fe}_1^{\mathrm{nb}}}}\right] \tag{11b}$$

$$\Delta g_z \cong 2\zeta^{\mathrm{Fe}}\left[\frac{(2\Gamma_{x^2-y^2}^{\mathrm{Fe}}\Gamma_{xy}^{\mathrm{Fe}} + \Gamma_{xz}^{\mathrm{Fe}}\Gamma_{yz}^{\mathrm{Fe}})^2}{\Delta_{\mathrm{Fe}_2^{\mathrm{nb}},\mathrm{Fe}_1^{\mathrm{nb}}}} + \frac{(2\Gamma_{xy}^{\mathrm{Fe}}\Xi_{x^2-y^2}^{\mathrm{Fe}} + \Gamma_{yz}^{\mathrm{Fe}}\Xi_{xz}^{\mathrm{Fe}})^2}{\Delta_{\pi_2^*,\mathrm{Fe}_1^{\mathrm{nb}}}}\right] \tag{11c}$$

It is worth noting that, because of the highly localized unpaired electron, the g-value expressions take the form of those for a covalently reduced mononuclear coordination complex. This is due to the nature of the orbital in which the excitations originate, which has very little electron density on the V ion. If we were to append the expressions for the nonbonding orbitals with a small fraction of V-based d-orbital character, ρ, the contribution to $\tilde{\mathbf{g}}$ would be on the order of $(\rho\Xi_{xz,yz}^{\mathrm{V}})^2$. Combining these expressions with the calculated orbital populations and energy levels, plus the free ion spin-orbit coupling constant for Fe^{I} ($\zeta^{\mathrm{Fe}} = 350\ \mathrm{cm}^{-1}$), results in $g_x = 2.014$, $g_y = 2.077$, and $g_z = 2.245$. From these expressions, it is evident that the deviation from the axial anisotropy is driven by energy differences of the π_1^*/π_2^* orbitals, the nondegenerate set of $\mathrm{Fe}^{\mathrm{nb}}$ configurations, and asymmetric covalency. This deviation from ideal C_3 symmetry can be induced by either crystal-packing interactions of the bulky ligand groups, or the $E\otimes e$ Jahn-Teller effect.[39] Experimentally, we observe two different sets of EPR parameters, which only differ in the largest g value. From this observation, we would expect the two distinct crystallographic sites to differ in a way that would vary the splitting of the $\mathrm{Fe}_1^{\mathrm{nb}}/\mathrm{Fe}_2^{\mathrm{nb}}$ orbitals. When the structures of the two sites are overlayed, it is evident that several small distortions create significant deviations between the two, which can lead to non-negligible changes in the ground- and excited-state energetics.[40] The echo-detected EPR spectrum of a solution of **1** (Figure S5) shows $\tilde{\mathbf{g}}$-tensor components that are nearly identical with those observed in the powder. However, in solution, we observe only one g_z component. This observation suggests that the multiple solid state structures are not intrinsic to the molecule and are instead induced by crystal packing forces.

■ CONCLUSIONS

The objective of this study was to investigate the electronic structure of a heterobimetallic compound featuring multiple bonds between two distinct first row transition metals. To

DOI: 10.1021/acs.inorgchem.8b00280
Inorg. Chem. 2018, 57, 5870−5878

achieve this, we have employed a combination of HFEPR, variable-field Mössbauer spectroscopy, and ELDOR-NMR, from which we could probe the magnetic properties as well as the hyperfine interactions present in **1**. We have investigated localization of the single unpaired electron and found that it resides in an Fe-based orbital containing ~77% d_{xy}-type and 23% d_{xz}-type character. We have also employed a new technique in the field of metal-metal bonding, ELDOR-NMR, through which we could examine the electron density present on the V site and quantify the small, axial $^{V}\tilde{\mathbf{A}}$ tensor, which was undetectable through other techniques. We additionally proposed a simple ligand field model to rationalize the physical origin of the $\tilde{\mathbf{g}}$-tensor anisotropy, which we hope will be useful in the interpretation of g factors in similar complexes.

■ ASSOCIATED CONTENT

Ⓢ Supporting Information

The Supporting Information is available free of charge on the ACS Publications website at DOI: 10.1021/acs.inorgchem.8b00280.

> Additional experimental and theoretical data including zero-field Mössbauer spectra, a comparison of distinct crystallographic sites, multifrequency EPR, ELDOR-NMR spectra, quantum chemical calculations, and input files (PDF)

■ AUTHOR INFORMATION

Corresponding Authors

*E-mail: thomasc@brandeis.edu.
*E-mail: sstoian@uidaho.edu.
*E-mail: shill@magnet.fsu.edu.

ORCID

Samuel M. Greer: 0000-0001-8225-3252
Christine M. Thomas: 0000-0001-5009-0479
Sebastian A. Stoian: 0000-0003-3362-7697
Stephen Hill: 0000-0001-6742-3620

Notes

The authors declare no competing financial interest.

■ ACKNOWLEDGMENTS

A portion of this work was performed at the National High Magnetic Field Laboratory (NHMFL), which is supported by the NSF Cooperative Agreement (DMR-1157490 and DMR-1644779) and the State of Florida. This work used the Extreme Science and Engineering Discovery Environment, which is supported by National Science Foundation (NSF) Grant ACI-1053575 as well as the High Performance Computing Center at Florida State University. The Mössbauer instrument was purchased through the NHMFL User Collaboration Grant Program (UCGP5064) awarded to Dr. Andrzej Ozarowski. S.M.G. acknowledges support from the NSF Graduate Research Fellowship Program (DGE-1449440). Support from the NSF (Grant DMR-1610226 to S.H.) and the Department of Energy's Basic Energy Sciences Catalysis Program (DE-SC0014151 awarded to C.M.T.) is also acknowledged. S.A.S. acknowledges partial support from the University of Idaho.

■ REFERENCES

(1) Cotton, F. A. Metal-Metal Bonding in $[Re_2X_8]^{2-}$ Ions and Other Metal Atom Clusters. *Inorg. Chem.* **1965**, *4*, 334−336.

(2) Clouston, L. J.; Bernales, V.; Cammarota, R. C.; Carlson, R. K.; Bill, E.; Gagliardi, L.; Lu, C. C. Heterobimetallic Complexes That Bond Vanadium to Iron, Cobalt, and Nickel. *Inorg. Chem.* **2015**, *54*, 11669−11679.

(3) Wu, B.; Wilding, M. J. T.; Kuppuswamy, S.; Bezpalko, M. W.; Foxman, B. M.; Thomas, C. M. Exploring Trends in Metal−Metal Bonding, Spectroscopic Properties, and Conformational Flexibility in a Series of Heterobimetallic Ti/M and V/M Complexes (M = Fe, Co, Ni, and Cu). *Inorg. Chem.* **2016**, *55*, 12137−12148.

(4) Carlson, R. K.; Odoh, S. O.; Tereniak, S. J.; Lu, C. C.; Gagliardi, L. Can Multiconfigurational Self-Consistent Field Theory and Density Functional Theory Correctly Predict the Ground State of Metal−Metal-Bonded Complexes? *J. Chem. Theory Comput.* **2015**, *11*, 4093−4101.

(5) Hernández-Sánchez, R.; Betley, T. A. Meta-Atom Behavior in Clusters Revealing Large Spin Ground States. *J. Am. Chem. Soc.* **2015**, *137*, 13949−13956.

(6) Cooper, B. G.; Napoline, J. W.; Thomas, C. M. Catalytic Applications of Early/Late Heterobimetallic Complexes. *Catal. Rev.: Sci. Eng.* **2012**, *54*, 1−40.

(7) Kuppuswamy, S.; Powers, T. M.; Krogman, J. P.; Bezpalko, M. W.; Foxman, B. M.; Thomas, C. M. Vanadium-iron complexes featuring metal-metal multiple bonds. *Chem. Sci.* **2013**, *4*, 3557−3565.

(8) Krogman, J. P.; Thomas, C. M. Metal-metal multiple bonding in C_3-symmetric bimetallic complexes of the first row transition metals. *Chem. Commun.* **2014**, *50*, 5115−5127.

(9) Wu, B.; Bezpalko, M. W.; Foxman, B. M.; Thomas, C. M. A heterobimetallic complex featuring a Ti−Co multiple bond and its application to the reductive coupling of ketones to alkenes. *Chem. Sci.* **2015**, *6*, 2044−2049.

(10) Clouston, L. J.; Siedschlag, R. B.; Rudd, P. A.; Planas, N.; Hu, S.; Miller, A. D.; Gagliardi, L.; Lu, C. C. Systematic Variation of Metal−Metal Bond Order in Metal−Chromium Complexes. *J. Am. Chem. Soc.* **2013**, *135*, 13142−13148.

(11) Eisenhart, R. J.; Clouston, L. J.; Lu, C. C. Configuring Bonds Between First-Row Transition Metals. *Acc. Chem. Res.* **2015**, *48*, 2885−2894.

(12) Prisecaru, I. WMOSS4 Mössbauer Spectral Analysis Software. http://wmoss.org/.

(13) Hassan, A. K.; Pardi, L. A.; Krzystek, J.; Sienkiewicz, A.; Goy, P.; Rohrer, M.; Brunel, L. C. Ultrawide Band Multifrequency High-Field EMR Technique: A Methodology for Increasing Spectroscopic Information. *J. Magn. Reson.* **2000**, *142*, 300−312.

(14) Stoll, S.; Schweiger, A. EasySpin, a comprehensive software package for spectral simulation and analysis in EPR. *J. Magn. Reson.* **2006**, *178*, 42−55.

(15) Stoll, S.; Britt, R. D. General and efficient simulation of pulse EPR spectra. *Phys. Chem. Chem. Phys.* **2009**, *11*, 6614−6625.

(16) Cruickshank, P. A.; Bolton, D. R.; Robertson, D. A.; Hunter, R. I.; Wylde, R. J.; Smith, G. M. A kilowatt pulsed 94 GHz electron paramagnetic resonance spectrometer with high concentration sensitivity, high instantaneous bandwidth, and low dead time. *Rev. Sci. Instrum.* **2009**, *80*, 103102-1−103102-15.

(17) Schweiger, A.; Jeschke, G. *Principles of Pulse Electron Paramagnetic Resonance*; Oxford University Press: Oxford, U.K., 2001.

(18) Cox, N.; Lubitz, W.; Savitsky, A. W-band ELDOR-detected NMR (EDNMR) spectroscopy as a versatile technique for the characterisation of transition metal−ligand interactions. *Mol. Phys.* **2013**, *111*, 2788−2808.

(19) Kaminker, I.; Wilson, T. D.; Savelieff, M. G.; Hovav, Y.; Zimmermann, H.; Lu, Y.; Goldfarb, D. Correlating nuclear frequencies by two-dimensional ELDOR-detected NMR spectroscopy. *J. Magn. Reson.* **2014**, *240*, 77−89.

(20) Wang, X.; McKay, J. E.; Lama, B.; van Tol, J.; Li, T.; Kirkpatrick, K.; Gan, Z.; Hill, S.; Long, J. R.; Dorn, H. C. Gadolinium Based Endohedral Metallofullerene $Gd_2@C_{79}N$ as a Relaxation Boosting Agent for Dissolution DNP at High Fields. *Chem. Commun.* **2018**, *54* (19), 2425−2428.

(21) Neese, F. The ORCA program system. *Wiley Interdiscip. Rev. Comput. Mol. Sci.* **2012**, *2*, 73−78.

(22) Frisch, M. J.; Trucks, G. W.; Schlegel, H. B.; Scuseria, G. E.; Robb, M. A.; Cheeseman, J. R.; Scalmani, G.; Barone, V.; Mennucci, B.; Petersson, G. A.; Nakatsuji, H.; Caricato, M.; Li, X.; Hratchian, H. P.; Izmaylov, A. F.; Bloino, J.; Zheng, G.; Sonnenberg, J. L.; Hada, M.; Ehara, M.; Toyota, K.; Fukuda, R.; Hasegawa, J.; Ishida, M.; Nakajima, T.; Honda, Y.; Kitao, O.; Nakai, H.; Vreven, T.; Montgomery, J. A., Jr.; Peralta, J. E.; Ogliaro, F.; Bearpark, M. J.; Heyd, J.; Brothers, E. N.; Kudin, K. N.; Staroverov, V. N.; Kobayashi, R.; Normand, J.; Raghavachari, K.; Rendell, A. P.; Burant, J. C.; Iyengar, S. S.; Tomasi, J.; Cossi, M.; Rega, N.; Millam, N. J.; Klene, M.; Knox, J. E.; Cross, J. B.; Bakken, V.; Adamo, C.; Jaramillo, J.; Gomperts, R.; Stratmann, R. E.; Yazyev, O.; Austin, A. J.; Cammi, R.; Pomelli, C.; Ochterski, J. W.; Martin, R. L.; Morokuma, K.; Zakrzewski, V. G.; Voth, G. A.; Salvador, P.; Dannenberg, J. J.; Dapprich, S.; Daniels, A. D.; Farkas, Ö.; Foresman, J. B.; Ortiz, J. V.; Cioslowski, J.; Fox, D. J. *Gaussian09*; Gaussian, Inc.: Wallingford, CT, 2009.

(23) Weigend, F.; Ahlrichs, R. Balanced basis sets of split valence, triple zeta valence and quadruple zeta valence quality for H to Rn: Design and assessment of accuracy. *Phys. Chem. Chem. Phys.* **2005**, *7*, 3297−3305.

(24) Becke, A. D. Density-functional exchange-energy approximation with correct asymptotic behavior. *Phys. Rev. A: At., Mol., Opt. Phys.* **1988**, *38*, 3098−3100.

(25) Perdew, J. P. Density-functional approximation for the correlation energy of the inhomogeneous electron gas. *Phys. Rev. B: Condens. Matter Mater. Phys.* **1986**, *33*, 8822−8824.

(26) The ORCA basis set CoreProp was used. This basis is based on the TurboMole DZ basis developed by Ahlrichs and co-workers.

(27) Romelt, M.; Ye, S.; Neese, F. Calibration of modern density functional theory methods for the prediction of ^{57}Fe Mössbauer isomer shifts: meta-GGA and double-hybrid functionals. *Inorg. Chem.* **2009**, *48*, 784−785.

(28) Mabbs, F. E.; Collison, D. *Electron Paramagnetic Resonance of d Transition Metal Compounds*; Elsevier: Amsterdam, The Netherlands, 1992.

(29) Hay, P. J.; Thibeault, J. C.; Hoffmann, R. *J. Am. Chem. Soc.* **1975**, *97*, 4884−4899.

(30) Drago, R. S. *Physical methods for chemists*; Surfside: Gainesville, FL, 1965.

(31) $\tilde{\mathbf{A}}_{\mathrm{Fc}} = A_{\mathrm{Fc}}\mathbb{I}_n$, where $\mathbb{I}_n$ is the identity matrix.

(32) Gütlich, P.; Bill, E.; Trautwein, A. *Mössbauer Spectroscopy and Transition Metal Chemistry: Fundamentals and Application*; Springer: Berlin, 2011.

(33) Tregenna-Piggott, P. L. W.; Spichiger, D.; Carver, G.; Frey, B.; Meier, R.; Weihe, H.; Cowan, J. A.; McIntyre, G. J.; Zahn, G.; Barra, A.-L. Structure and Bonding of the Vanadium(III) Hexa-Aqua Cation. 1. Experimental Characterization and Ligand-Field Analysis. *Inorg. Chem.* **2004**, *43*, 8049−8060.

(34) $A = 1$ MHz corresponds to $A/g_n\beta_n = 0.729$ T.

(35) Sinnecker, S.; Neese, F.; Noodleman, L.; Lubitz, W. Calculating the Electron Paramagnetic Resonance Parameters of Exchange Coupled Transition Metal Complexes Using Broken Symmetry Density Functional Theory: Application to a Mn$^{\mathrm{III}}$/Mn$^{\mathrm{IV}}$ Model Compound. *J. Am. Chem. Soc.* **2004**, *126*, 2613−2622.

(36) Neese, F. A critical evaluation of DFT, including time-dependent DFT, applied to bioinorganic chemistry. *J. Biol. Inorg. Chem.* **2006**, *11*, 702−711.

(37) Gorelsky, S. I. Complexes with a Single Metal−Metal Bond as a Sensitive Probe of Quality of Exchange-Correlation Functionals. *J. Chem. Theory Comput.* **2012**, *8*, 908−914.

(38) Neese, F.; Solomon, E. I. Interpretation and Calculation of Spin Hamiltonian Parameters in Transition Metal Complexes. *Magnetism: Molecules to Materials*; Wiley-VCH Verlag GmbH & Co. KGaA: Berlin, 2003; pp 345−466.

(39) Bersuker, I. B. *The Jahn−Teller Effect*; Cambridge University Press: Cambridge, U.K., 2006.

(40) Stoian, S. A.; Smith, J. M.; Holland, P. L.; Münck, E.; Bominaar, E. L. Mössbauer, Electron Paramagnetic Resonance, and Theoretical Study of a High-Spin, Four-Coordinate Fe(II) Diketiminate Complex. *Inorg. Chem.* **2008**, *47* (19), 8687−8695.

DOI: 10.1021/acs.inorgchem.8b00280
Inorg. Chem. 2018, 57, 5870−5878